Materials Advances

PAPER

Check for updates

Engineered Mn–Zn-doped ferrite nanomaterials: exploring magnetothermal effects for cancer treatment

Rushikesh Fopase, [iD] [a] Krishna Priya Hazarika, [b] J. P. Borah [b] and Lalit M. Pandey [iD] *[a]

The present work investigates the potential of Mn–Zn-doped ferrite (FMZ) nanoparticles for magnetic hyperthermia, focusing on the optimization of their magnetic characteristics to enhance their heat generation efficiency. The co-precipitation route was used to design FMZ ($Mn_xZn_{1-x}Fe_2O_4$) nanomaterials with x = 0, 0.25, 0.50, 0.75, and 1.0. Redshifts in their inverse spinel diffraction patterns confirmed the doping. Functional group analysis further verified the interactions of Zn and Mn within the ferrite lattice, while X-ray photoelectron spectroscopy (XPS) revealed their occupancy. The single-domain nature of the FMZ nanoparticles showed a spherical particle, with size varying linearly from 13.6 ± 2 to 15.7 ± 3 nm with an increase in the Mn content. Magnetic characterization revealed the linear relation of magnetization and Mn content with the superparamagnetic nature of the synthesized FMZ samples. The FMZ0.75 sample showed the highest magnetic saturation (M_S) value of 38.90 emu g^{-1} among the FMZ samples. The specific absorption rate (SAR) values for the FMZ0.75 sample at 1, 3, and 5 mg mL^{-1} were 173.24, 107.12, and 105.42 W g^{-1}, respectively. Notably, FMZ0.75 at 3 mg mL^{-1} reached hyperthermia temperature within 5 minutes. Furthermore, a peak function elucidated the interrelationship among particle size, M_S, and SAR values, identifying an optimum particle size of 14.7 nm and an Mn fraction of 0.7. Cytocompatibility assays confirmed the suitability of FMZ samples against HEK-293 cells for the tested concentrations of up to 5 mg mL^{-1}. Simulated hyperthermia studies revealed a significant reduction (35%) in the viability of the A549 cancer cell line, underlining the selective efficacy of FMZ nanomaterials. Considering the observed effective cytocompatibility and SAR values, FMZ samples can be effectively used for hyperthermia and related adjuvant therapy, such as chemotherapy for drug delivery applications.

1. Introduction

Cancer is a highly focused research area due to its high impact on human life in terms of social and economic factors. The currently applied treatment strategies are more inclined towards advancements with fewer side effects. Hyperthermia is one of the alternative strategies to conventional cancer treatment methods. This treatment procedure involves the exposure of an injected tissue or organ to an elevated temperature in the range of 42–47 °C.[1] The heat generated is responsible for damaging the proteins and cellular components within cancer cells. At the same time, healthy cells or tissues can handle stress by activating heat shock proteins.[2]

Hyperthermia is a non-invasive and precision-controlled approach for cancer treatment that minimizes side effects. Additionally, the application of hyperthermia as an adjuvant therapy to chemotherapy or radiotherapy increases the potency of the treatment. Various magnetic nanoparticles (MNPs) are being explored for their potential therapeutic applications through hyperthermia.[3] The heat generated by MNPs can be applied for synergistic effects using hyperthermia and drug delivery using thermosensitive polymers.[4,5] The system provides a synergistic effect through heat-induced hyperthermia and controlled drug release, enhancing chemotherapeutic efficacy against various cancer cell lines.

A high-frequency alternating magnetic field (AMF) generates heat from MNPs *via* hysteresis and relaxation losses (Néel and Brownian relaxation).[6] The heating efficiency of MNPs depends on their magnetization, particle size, and concentration, and the parameters of the applied field.[7] Among the MNPs, iron oxide nanoparticles, especially ferrite nanoparticles, have been widely used candidates for biological

[a] Bio-interface & Environmental Engineering Lab, Department of Biosciences and Bioengineering, Indian Institute of Technology Guwahati, Assam, 781039, India. E-mail: lalitpandey@iitg.ac.in; Fax: +91-361-258-2249; Tel: +91-361-258-3201

[b] Nanomagnetism Group, Department of Physics, National Institute of Technology Nagaland, Dimapur, Nagaland, 797103, India

applications due to their biocompatibility and tunable magnetic properties.[8]

Spinel ferrites (MFe_2O_4, where M: divalent metal ion (e.g., Fe^{2+}, Zn^{2+}, Mn^{2+}, and Co^{2+})) with a face-centered cubic (fcc) crystal structure belonging to the $Fd\bar{3}m$ (227) space group, have eight molecules per unit cell. Based on the ion distribution at the tetrahedral (A sites) and octahedral (B sites) sites, the intrinsic properties of ferrites can be tuned. Zn and Mn co-doped ferrites are being explored for their considerable significance in magnetic hyperthermia applications. The distribution of the Zn and Mn ions in the lattice enables fine-tuning of their magnetic properties, such as magnetization, which are crucial for achieving adequate heating capability. Zn ions preferentially occupy the tetrahedral (A) sites in the spinel structure and reduce the antiferromagnetic coupling between the A and B sites due to their non-magnetic nature.[9] This redistribution reduces the magnetic anisotropy and contributes to the enhancement of the superparamagnetic behavior of the ferrites by facilitating the formation of single-domains.[10] Further, the Mn ions contribute to the overall magnetic moment and improve the thermal stability of the ferrites.[11,12] Thus, by tuning the suitable molar ratio of Zn and Mn, the performance of ferrites can be improved for magnetic hyperthermia.

For efficient hyperthermia, high specific absorption rate (SAR) values are desired. In the study by de Mello et al., Zn–Mn-doped magnetite nanomaterials were synthesized, yielding a maximum SAR value of 37.7 W g^{-1} (f = 112 kHz and H = 25 mT) for 0.4 mol faction of (Zn + Mn) ions.[13] Another study reported an SAR value of 88 W g^{-1} (f = 500 kHz and H = 4 kA m^{-1}) for $Mn_{0.07}Zn_{0.03}Fe_2O_4$ nanomaterials synthesized through the co-precipitation method.[14] Similarly, $Mn_{0.1}Zn_{0.09}Fe_2O_4$ nanomaterials exhibited a specific loss of power value of 107.79 W g^{-1} (f = 316 kHz and H = 35.2 kA m^{-1}) for 1 mg mL^{-1}.[15] Despite the improvements, the reported SAR values remained constrained due to the limited optimization of the dopant fractions.

The present work focuses on the synthesis and evaluation of Mn–Zn co-doped ferrites for magnetic hyperthermia applications. The FMZ nanomaterials were synthesized using varying amounts of Mn and Zn (Table 1) using the co-precipitation method and characterized for their physical properties, including phase formation and magnetization. The heating capability of the samples was tested under an AMF to determine their suitability for hyperthermia. Additionally, the biocompatibility of the synthesized ferrites was analyzed to confirm their

biological safety. The effects of hyperthermia-induced temperature on cancer and healthy cells were also studied to assess their therapeutic efficacy and safety.

2. Materials and methods

2.1. Materials

All the chemicals used were purchased from HiMedia Laboratories, India. Ferric chloride ($FeCl_3\cdot 6H_2O$), zinc chloride ($ZnCl_2$), and manganese chloride ($MnCl_2\cdot 4H_2O$) were used as precursors. Sodium hydroxide (HiMedia) was used as a reducing agent. All solutions were prepared in deionized water.

2.2. Synthesis of Mn- and Zn-doped iron oxide nanoparticles

The Mn and Zn-doped iron nanoparticles were prepared using the co-precipitation method due to its simplicity, scalability, and reproducibility.[13] The Fe^{3+} to dopant ion (Mn^{2+}/Zn^{2+}) ratio was kept at 2 : 1 by completely replacing the Fe^{2+} ions in the formula. The dopant content was distributed in different ratios of Mn and Zn and coded as FZ, FMZ0.25, FMZ0.5, FMZ0.75, and FM for an increase in Mn content from 0 to 1 fraction, as listed in Table 1. The respective precursors were added to 50 mL deionized water and mixed using a magnetic stirrer at 80 °C at the stirring speed of 500 revolutions per minute. The initial pH was estimated to be in the range of 2–3. After 30 min, a 2 M NaOH solution was added dropwise to the reaction mixture until the reaction pH reached around the value of 11. The solution was stirred for 3 h after adding NaOH and left to settle overnight. The precipitate was washed several times with deionized water and ethanol and dried at 80 °C. After drying, the samples were ground to a powder and calcinated at 1150 °C for 4 h.

2.3. Characterization of Mn- and Zn-doped iron oxide nanoparticles

2.3.1. Physical characterization. The crystallite structure and phases of the synthesized samples were analyzed through an X-ray diffractometer (XRD) (Rigaku, SmartLab) using CuKα as the X-ray source at the wavelength (λ) of 1.54 Å in the 2θ range of 20–80°. The crystallite sizes of the samples were calculated using the Debye–Scherrer equation (eqn (1)), as follows:

$$D = \frac{k\lambda}{\beta\cos\theta} \tag{1}$$

where D is the crystallite size, k is the shape factor (≈ 0.9), λ is the X-ray wavelength, β is full width at half maximum intensity of the peak, and θ is the diffraction angle. The chemical and functional groups of the synthesized samples were assessed by Fourier transform infrared spectroscopy (FTIR) (Spectrum Two, PerkinElmer) and high-resolution laser micro Raman system (He–Ne laser 488 nm) (LabRAM HR800, HORIBA). The chemical states of the dopants were analyzed using X-ray photoelectron spectroscopy. The morphology and particle size of the samples were analyzed using a field emission scanning electron microscope (FESEM) (Sigma300, Zeiss) and a field emission

Table 1 Molar ratios used for the synthesis of Mn–Zn doped iron nanoparticles

Code	Fe	Mn	Zn
FZ	2	0	1
FMZ0.25	2	0.25	0.75
FMZ0.5	2	0.5	0.5
FMZ0.75	2	0.75	0.25
FM	2	1	0

transmission electron microscope (FETEM) (JEOL 2100F). The elemental compositions of the samples were determined using energy-dispersive X-ray spectroscopy (EDX) (Sigma, Zeiss).

2.3.2. Magnetic characterization. The magnetic characteristics of the prepared samples were analyzed using a vibrating sample magnetometer (VSM) (Lakeshore, 7410) under an applied magnetic field. The heat generation abilities of the prepared samples were assessed through an 8-turn coil induction heating unit (EASYHEAT-8310, Ambrell UK). Different sample concentrations (1, 3, and 5 mg mL^{-1}) in deionized water were subjected to an applied field amplitude (H) of 12.89 kA m^{-1} and frequency (f) of 336 kHz for 15 min. The increase in the temperature of the sample solutions was used to estimate the heat generation abilities of the samples in terms of specific absorption rate (SAR) values. For the normalization of the SAR values with different frequency and field values used by various researchers for various materials, intrinsic loss power (ILP) can be used as a parameter.

2.3.3. Biological characterization. The cytocompatibility of the synthesized ferrite nanoparticles towards human embryonic kidney cells (HEK-293) was analyzed through the MTT (3-(4,5-dimethylthiazolyl-2)-2,5-diphenyltetrazolium bromide) assay. The cells were cultured in Dulbecco's modified Eagle medium (DMEM, Himedia) with 10% fetal bovine serum (FBS, Himedia) in a CO$_2$ incubator (Galaxy$^{\circledR}$ 170 S, Eppendorf) at 37 °C in 5% CO$_2$. For the experiment, 10^4 cells per well were seeded in a 96-well plate with different sample concentrations (5, 3, 1, 0.5, 0.1, and 0.05 mg mL^{-1}). No samples were added to the control wells, which served as the negative control, while the wells with only media were used for background absorbance. All experiments were performed in triplicate. The plates were incubated in a CO$_2$ incubator for 2 and 4 days. After incubation, the spent medium in the plates was replaced with fresh medium containing MTT solution (0.5 mg mL^{-1}). After 4 h, the medium was replaced with 100 μL dimethyl sulfoxide (DMSO) to dissolve the formed formazan crystals. The absorbance of the observed purple color in the plates was recorded at 570 nm using a multi-plate reader (FLUOstar Omega, BMG

Labtech). The cell viability was determined by comparing the absorbance of the control wells and sample wells, as follows (eqn (2)):

$$\text{Cell viabilty } (\%) = \frac{\text{Abs}_{\text{sample}}}{\text{Abs}_{\text{control}}} \times 100 \quad (2)$$

The extent of the heat susceptibility of normal and cancer cells, HEK-293 and A549 (human lung cancer cell line), respectively, was determined by incubating the cells under hyperthermia conditions at 45 °C for 20 min. The control plates were incubated at 37 °C during the experiment. After the hyperthermia treatment, the plates were incubated in CO$_2$ for 24 h. The cell viability was determined using the MTT assay, as explained above.

3. Results and discussion

3.1. Phase analysis

The synthesized samples were analyzed for the formed phase using XRD, as illustrated in Fig. 1a. The diffractogram of the parent crystal system of Fe$_3$O$_4$ with an inverse spinel ($Fd\bar{3}m$, 227) structure exhibited characteristic peaks at 2θ values of 35.50° (311), 43.17° (400), 57.06° (511), and 62.65° (440) (ICDD No. 01-088-0866).[16] The characteristic peaks shifted towards lower 2θ values due to the doping of Zn and Mn ions. In the case of the Zn-only doped FZ sample, the (311) peak shifted to 35.30°, indicating the expansion of its lattice, which prominently further increased for the Mn-only doped FM samples with a peak shift to 34.92°. The lattice expansion of the cubic spinel system was evident by the variation in the lattice parameter values. The parent Fe$_3$O$_4$ crystal system revealed the cubic lattice parameter values ($a = b = c$) of 8.383 Å (ICDD No. 01-088-0866),[16] which increased to 8.432 Å for the FZ samples and 8.513 Å for the FM samples. The variation in the lattice parameter values was attributed to the different ionic radii of the constituents, $i.e.$, Zn^{2+} (0.74 Å) and Mn^{2+} (0.80 Å).[17] Further, the diffraction patterns of the FMZ0.25, FMZ0.5, and FMZ0.75 samples, with doping of Mn and Zn ions as Mn$_x$Zn$_{1-x}$Fe$_2$O$_4$
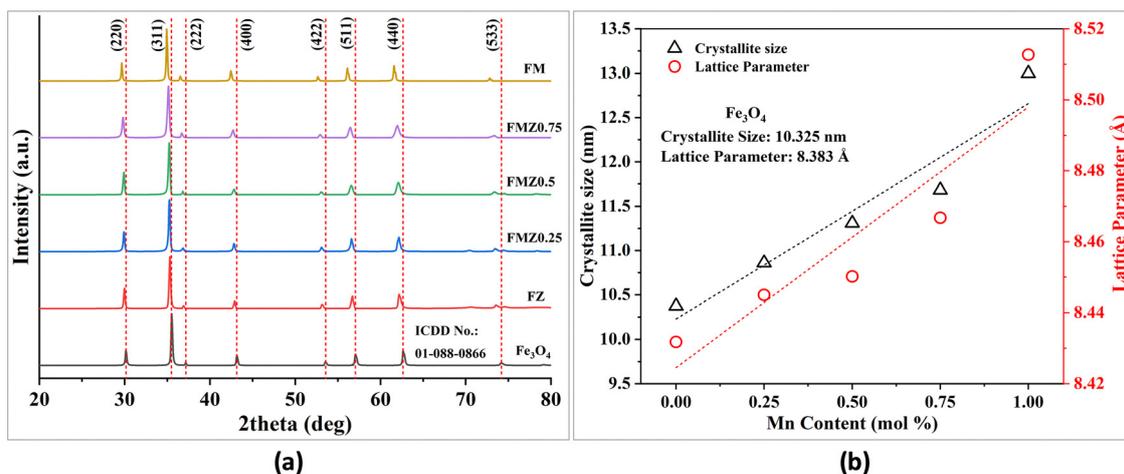

Fig. 1 (a) X-ray diffractogram and (b) variation in the crystallite size and lattice parameter values of Zn and Mn-doped ferrite samples.

(x = 0.25, 0.5, 0.75), showed a shift towards lower diffraction angle positions. Fig. S1 illustrates the lower angle-shifted diffractogram for the FMZ samples corresponding to the (311) plane, confirming the successful incorporation of the dopants. The variation in lattice parameters showed a progressive increment with an increase in Mn^{2+} content, indicating the effects of Mn incorporation on the lattice structure.[18] The lattice parameter values were observed in the intermediate range of the FZ and FM samples. The correlation between the Mn content and the lattice parameter is presented in Fig. 1b. The increasing trend of the lattice parameter was reflected in the increased unit cell volumes of the FMZ samples, giving 599.454, 602.271, 603.387, 606.946, and 616.881 Å^3 for the FZ, FMZ0.25, FZM 0.5, FMZ0.75, and FM samples, respectively.

The synthesized samples exhibited the desired phases with the dopant amount, as confirmed by their match with the ICDD standard files (FZ: 01-076-6123,[19] FMZ0.25: 01-074-2399, FMZ0.5: 01-086-8880, FMZ0.75: 00-069-0164, and FM: 01-075-3192).[20] The observed phases were also confirmed for the elemental compositions using energy-dispersive X-ray analysis, as shown in Fig. S2. The atomic percentages of the elements corresponded well with the doping amount of Zn and Mn. Further, the crystallite sizes of the FMZ samples, calculated using the Debye–Scherrer formula, demonstrated an increasing trend with an increase in Mn content, as illustrated in Fig. 1b. Compared to the crystallite size of 10.33 nm for the parent Fe_3O_4 system, the FZ sample showed an increased crystallite size of 10.37 nm, whereas the FM sample demonstrated the largest crystallite size of 13.00 nm. The crystallite sizes observed in the obtained crystallites were almost similar to the particle sizes of the FMZ samples estimated through the FESEM analysis, indicating the appearance of single magnetic domain-like characteristics, as discussed later.[10] The lower diffraction position-shifted characteristic peaks observed in the inverse spinel structure, and the variation in lattice parameters confirmed the successful doping of Mn and Zn in the FMZ samples. The absence of significant secondary phases indicates the preservation of the lattice structure, ensuring the native magnetic features required for induction heating applications.

3.2. Functional group analysis

3.2.1. FTIR characterization. The analysis of chemical functional groups in the synthesized FMZ samples *via* FTIR is presented in Fig. 2a. The FTIR spectra unveiled two prominent peaks in the characteristic wavenumber region of 1000–400 cm^{-1} for the FMZ samples. The peak at approximately ν_2 433 cm^{-1} indicated the presence of the stretching vibration of Fe^{3+}–O bonds at the B site in the lattice of the inverse spinel structure of the FMZ samples.[21] Another peak near 535 cm^{-1} was observed, corresponding to the Fe^{3+}/Fe^{2+}–O interactions at the A-sites of the lattice.[22] The doping of Zn and Mn in the crystal preferentially replaces Fe^{3+} at the A site, indicating the M–O interaction through the slight shift in the peaks.[23] The tetrahedral peaks were observed to shift towards higher wavenumbers with an increase in the Zn content, indicating stronger Zn–O bonds (sample FZ: tetrahedral peak at 540 cm^{-1}) compared to Mn–O interactions (sample FM: tetrahedral peak at 532 cm^{-1}).[21] The FMZ0.25, FMZ0.5, and FMZ0.75 samples exhibited peaks in the range of 535 to 537 cm^{-1}, indicating the influence of the dopant distribution. No significant variations were observed for the octahedral peaks, except for the FMZ0.75 sample, which showed a peak at ν_2 430 cm^{-1}, suggesting potential lattice distortion due to mixed doping. The doping of Mn and Zn induced lattice disturbances due to their size differences.[24] The higher ionic radius of Mn^{2+} (0.80 Å) caused a decrease in the lattice symmetry, leading to a weaker Mn–O bond at lower wavenumbers. However, the Zn content increased the lattice symmetry owing to its small ionic radius (0.74 Å), as evidenced by the peaks at higher wavenumbers. The slight shift in the octahedral bonds to the wavenumber of ν_2 434 cm^{-1} indicated the increased stability of the Fe–O bonds with Zn content.[21]

3.2.2. Raman characterization. Group theory predicts five first-order Raman-active modes, *i.e.*, $1A_{1g}$, $1E_g$, and $3T_{2g}$, for an inverse spinel cubic structure, which helps explore the
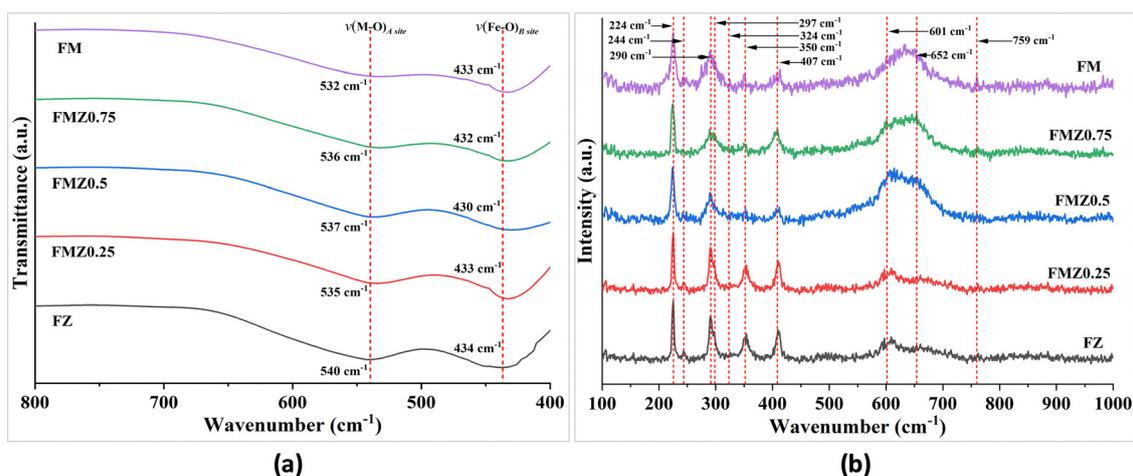

Fig. 2 (a) FTIR and (b) Raman spectra of Mn- and Zn-doped ferrite nanoparticles illustrating their chemical functional groups.

molecular structure of ferrite nanoparticles.[22] The A_{1g} mode dominates the spectrum, corresponding to the symmetric stretching vibration in the range of 590–710 cm^{-1} for the tetrahedral site.[25] At the same time, the $T_{2g}(1)$, $T_{2g}(2)$, and $T_{2g}(3)$ modes correspond to translational motion, asymmetric bending, and asymmetric stretching at the octahedral sites within the wavenumber range of 180–220, 450–520, and 500–590 cm^{-1}, respectively.[22] The peaks for the E_{1g} mode appeared at around 250–360 cm^{-1}, representing the symmetric ending of oxygen ions with Fe ions at both the tetrahedral and octahedral sites.[26] A comparison of the observed Raman spectra of the FMZ sample with that of the parent crystal system is shown in Fig. 2b.

The FMZ samples exhibited peaks for the E_{1g} mode between 242 and 291 cm^{-1}, signifying the Fe–O bonds at the two interacting sites, A and B.[22] The peak at 224 cm^{-1} for all the FMZ samples indicates translational motion associated with $T_{2g}(1)$.[27] In the FM and FZ samples analysis, shoulder peaks were observed at 275 and 297 cm^{-1}, respectively, indicating anti-symmetric distortions at the octahedral sites.[23] The variation in the peak positions for FM and FZ is possibly due to the difference in ionic size between Mn and Zn. Further, broadened peaks in the A_{1g} range were observed for all the samples, which are attributed to the overlapping Fe–O, Mn–O, and Zn–O interaction vibrations.[25] The deconvoluted peaks at 601, 631, 652, and 670 cm^{-1} correspond to the Fe–O stretching at the octahedral and tetrahedral sites, with shifts and broadening due to Zn and Mn substitution.[22] Furthermore, the FM and FZ samples exhibited a blueshift and redshift in the A_{1g} region of their Raman spectrum at a wavenumber of 632 cm^{-1} and 610 cm^{-1}, respectively. The opposite shift patterns arise due to the differing effects of the dopants on the Fe–O bond stiffness. The incorporation of Mn^{2+} increased the Fe–O strength, thus increasing the vibrational frequency to give a blueshift; in contrast, the addition of Zn^{2+} weakened the Fe–O bond and reduced the vibrational frequency, resulting in redshift.[28] The variations in the lattice are consistent with the obtained peak shifts in the XRD patterns. The shifts in the A_{1g} mode region indicate the successful doping and are sensitive to the magnetic ordering within the crystal.[29] Thus, the varying structural characteristics can be correlated with the magnetic properties of the FMZ samples (discussed in a later section). The variations in the peaks in the Raman spectrum of the ferrites with different dopants indicated the incorporation of Zn and Mn in the ferrite lattice with inverse spinel symmetry.

3.3. X-ray photoelectron spectroscopy characterization

The chemical states and elemental composition of the FMZ0.75 sample were analyzed using the XPS technique. The XPS survey spectrum of the FMZ0.75 sample, recorded in the range of 0 to 1300 eV (Fig. 2S), confirms the successful doping of Zn and Mn into the ferrite system. The detailed photoelectron spectra for the Fe 2p, Mn 2p, Zn 2p, and O 1s regions are shown in Fig. 3(a and d), respectively, providing further insight into the electronic structure and chemical environment of the sample.

The photoelectron spectrum for Fe 2p showed two major asymmetric peaks for Fe $2p_{3/2}$ (711.10 eV) and Fe $2p_{1/2}$ (725.35 eV) with the doublet spacing of 13.68 eV, indicating the formation of the Fe_3O_4 structure (Fig. 3a).[30] The peak for Fe $2p_{3/2}$ was contributed by the two deconvoluted peaks at 709.89 eV and 712.37 eV, highlighting the different chemical environments of the Fe ions in the spinel lattice. The peak at 709.89 eV arose due to the Fe^{3+} ions at octahedral sites, a characteristic of spinel ferrites. Alternatively, the peak at a higher energy at 712.37 denoted Fe^{3+} bonded with a hydroxyl group, suggesting the surface interactions.[31] The satellite peak at 719.55 eV corresponding to Fe $2p_{3/2}$ confirmed the presence of the Fe^{3+} state in the vicinity of the surface.[32] In the Mn 2p spectrum, two major peaks for Mn $2p_{3/2}$ and Mn $2p_{1/2}$ were observed, as shown in Fig. 3b. Deconvolution of the Mn $2p_{3/2}$ peak revealed three peaks at 640.08 eV for tetrahedral Mn^{2+}, 641.38 eV for octahedral Mn^{3+}, and 642.89 eV for Mn cations associated with a hydroxyl group in the structure.[30] The combined peak for Mn $2p_{1/2}$ was contributed by the two peaks corresponding to tetrahedral Mn^{2+} at 651.93 eV, octahedral Mn^{3+} at 653.29 eV, and 655.35 eV for possible Mn^{4+} configurations.[18] The two satellite peaks at 645.99 eV and 661.14 eV indicated the high-energy spins in the Mn^{2+} spin state.[33] The peak at 645.99 eV indicated the presence of Mn^{2+} on the surface of the particle.[32] The observed peaks indicated the occupation of both the tetrahedral and octahedral sites by Mn^{2+} due to its higher dopant amount.

Further, the photoelectron spectrum for Zn 2p (Fig. 3c) confirmed the incorporation of the Zn ions in the ferrite lattice. The major peaks at 1021.58 eV and 1025.44 eV confirmed the presence of Zn^{2+} at the tetrahedral sites.[32] The low-energy peak at 1020.80 eV was attributed to the distorted tetrahedral environment due to other dopant ions. Additionally, the Zn $2p_{1/2}$ peak at 1044.42 eV was attributed to Zn^{2+} ions in the tetrahedral sites, while the satellite peak at 1048.07 eV indicated surface Zn species associated with tetrahedral coordination.[34] Fig. 3d illustrates the O 1s spectrum, providing insight into the oxygen environment in the structure. The peak at 529.72 eV was attributed to lattice oxygen (O^{2-}), forming metal–oxygen (M–O) bonds with Fe, Mn, and Zn ions. The peak at 531.65 eV corresponded to surface hydroxyl groups (OH^-).[32] The peaks at 532.64 eV and 533.69 eV represented adsorbed oxygen species or hydroxyl groups, likely originating from surface-bound water molecules or chemisorbed oxygen.[35]

The XPS analysis confirms the presence of Mn and Zn in the ferrite samples and their distinct chemical states, and the site-specific binding energies for ions suggest their likely incorporation in the spinel ferrite lattice of the FMZ0.75 sample. The Fe ions predominantly occupied the octahedral sites and the Zn ions occupied the tetrahedral sites, while Mn showed mixed-site occupancy with tetrahedral and octahedral contributions. The cationic distribution plays a crucial role in optimizing the magnetic properties for magnetic hyperthermia applications. The modified magnetic coupling introduces controlled anisotropy, enhancing the thermal dissipation.[36] Also, the reduced super–exchange interaction between the two sites refines the
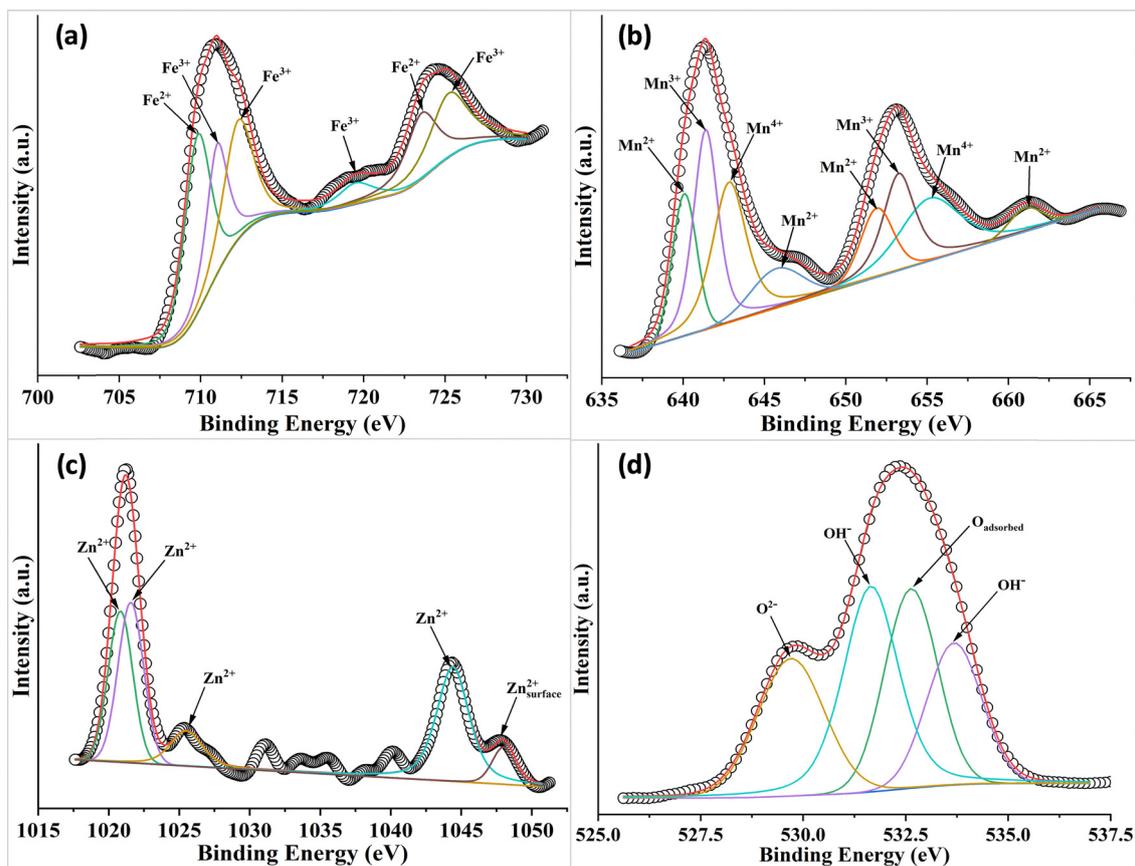
Fig. 3 X-ray photoelectron spectra of the FMZ0.75 sample illustrating (a) Fe 2p, (b) Mn 2p, (c) Zn 2p, and (d) O 1s peaks.

high-frequency magnetic relaxation and moderate coercivity (discussed later), which is essential for efficient magnetic hyperthermia.[37] Further, the peaks associated with surface hydroxyl groups and adsorbed oxygen species (Fig. 3d) highlight the influence of doping on surface chemistry, indicating enhanced interactions at the particle surface. These results emphasize the role of Mn and Zn doping in modifying the structural, electronic, and surface properties of the ferrite system.

3.4. Particle characteristics: morphology, particle size, and surface charge

The surface morphology and structure of the synthesized FMZ nanoparticles were revealed by FESEM analysis, as shown in Fig. 4(a–e). All the FMZ samples showed a spherical shape with a highly aggregated grain structure. The particle size was measured using the ImageJ software. The particle sizes of the samples were observed to increase with an increase in the Mn content, similar to the crystallite sizes determined through XRD analysis. The particle sizes estimated through the normal distribution histograms for the FZ, FMZ0.25, FMZ0.5, FMZ0.75, and FM samples were 13.6 ± 2, 13.9 ± 2, 14.1 ± 2, 14.8 ± 3, and 15.7 ± 3 nm, respectively. The increased particle was attributed to the changed lattice parameters and crystallite sizes due to the dopants (Fig. S3). Further, the particle

morphology of the FMZ0.75 sample was explored using FETEM, as shown in Fig. 4(f). The micrograph suggested the sphere-like morphology of this sample with aggregation. The particle size of 13.8 ± 4 nm was calculated using the ImageJ software with a histogram illustrating the distribution. Several studies have reported an increase in the particle size of Zn ferrites when doped with Mn. For example, Soltanpour et al. reported that the particle sizes Zn-doped Fe_3O_4 and Mn-doped Fe_3O_4 are 33.44 nm and 45.26 nm, respectively, indicating the effects of the dopant size.[21] Similarly, in another example, Kogulakrishnan et al. reported a decrease in particle size when Mn ferrite nanoparticles were doped with Zn.[38] The observed particle sizes are similar to the crystallite sizes, indicating the possible single-domain characteristics. Generally, Fe_3O_4 nanoparticles less than 20 nm are considered single-domain,[39] exhibiting very low coercivity, and are ideal for magnetic hyperthermia applications. The synthesized FMZ samples with the optimized particle size and H_C values suggest their suitability for safe and efficient induction heating-like applications.[12]

Further, the hydrodynamic diameters of the FMZ samples in Milli-Q water were estimated using a particle size analyzer through the intensity-based distribution, as illustrated in Fig. S4. Similar to the particle sizes, the hydrodynamic diameters gradually increased (from 29.2 nm to 35.1 nm) with an increase in Mn content, indicating the influence of the dopants on the
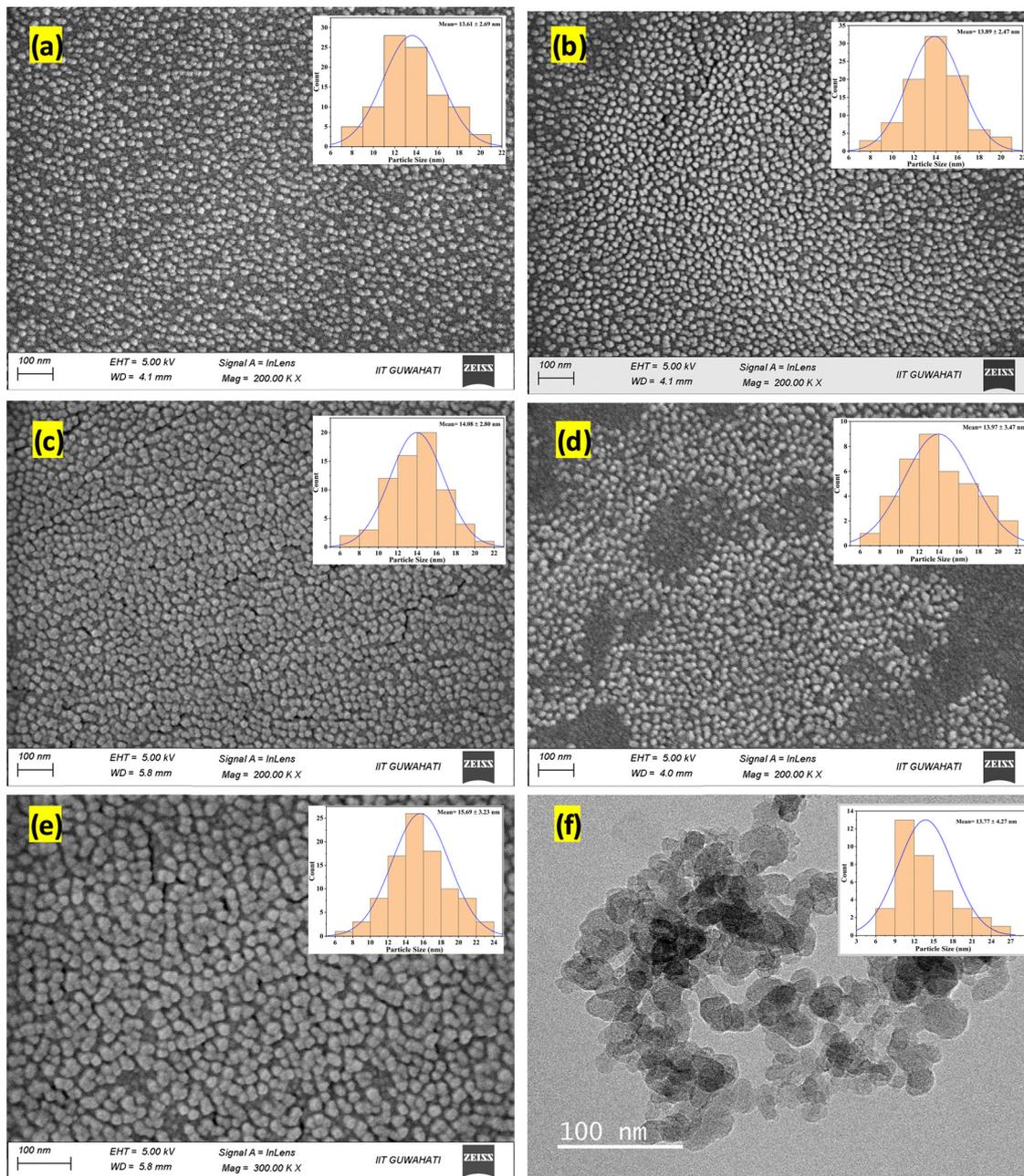
Fig. 4   FESEM micrographs of FMZ samples: (a) FZ, (b) FMZ0.25, (c) FMZ0.5, (d) FMZ0.75, and (e) FM. (f) FETEM micrograph and particle distribution of the FMZ0.75 sample.

particle surface chemistry and interfacial interactions. Given that the XPS analysis indicated the presence of Mn ions on the surface, they affected the surface properties to add a hydration layer on the particle surface. Also, the presence of surface hydroxyl groups leads to increased water adsorption and hydrodynamic layers. Further, the increase in magnetization values (discussed later) led to particle clustering and was highlighted as an increase in the hydrodynamic diameter. In the case of the FM sample with low magnetic saturation, the highest hydrodynamic diameter of 35.1 nm was attributed to its larger particle size and substantial hydration layer. The FZ sample

with the smallest particle size exhibited the minimum hydrodynamic size of 29.2 nm, indicating its minimal aggregation due to lower magnetization and limited interparticle interactions. The obtained results are in good correspondence with the study by Nasrin et al., where the hydrodynamic diameters of the MnZn ferrites increased with an increase in Mn content.[40]

The surface charges on the FMZ samples were determined using zeta potential, which showed a decreasing pattern with an increase in Mn content. The FZ sample showed the highest surface charge of −28.79 mV, indicating its high colloidal stability and justifying its smaller hydrodynamic diameter.

The surface charge and hydrodynamic size can be related to the stability theory for colloidal dispersions proposed by Derjaguin, Landau, Verwey, and Overbeek, referred as the DLVO theory.[41] The high surface charge, i.e., electrostatic repulsion, creates a significant energy barrier, preventing particle aggregation, and thus giving a smaller hydrodynamic diameter. The balance between van der Waals attraction and electrostatic repulsion determines colloidal stability. With a reduction in the surface charge, attraction forces overcome the repulsion energy barrier, resulting in particle clustering and a larger hydrodynamic size. The FMZ samples exhibited progressively decreasing surface charges to -23.71, -17.33, and -12.98 mV for the FMZ0.25, FMZ0.5, and FMZ0.75 samples, respectively. The reduction in the surface charge was reflected by the increase in the hydrodynamic diameter of the respective samples. The FM sample displayed the lowest surface charge of -9.53 mV, reflecting the colloidal instability and aggregation tendency, justifying the higher hydrodynamic diameter relative to the other FMZ samples.

3.5. Magnetic characterisation

The magnetic characteristics, such as saturation magnetization (M_S), coercivity (H_C), and remanence field (M_R), of the FMZ samples were measured using VSM, as shown in Fig. 5. All the FMZ samples exhibited superparamagnetic properties, with the FZ sample exhibiting slightly higher H_C and M_R values. The magnetization curves showed higher saturation values, with the Mn ions replacing the Zn ions. The FMZ0.25 sample showed an M_S value of 18.32 emu g^{-1}, while the FMZ0.75 sample, with the least amount of Zn, showed the maximum M_S value of 38.90 emu g^{-1}. The FZ sample with Zn-only dopant showed saturation magnetization at 9.67 emu g^{-1} due to the diamagnetic nature of the Zn ions. Alternatively, for the FM sample, the M_S value was observed to be 14.72 emu g^{-1}. Further, the FMZ samples exhibited lower H_C and M_R values, highlighting their superparamagnetic nature required for biomedical

Fig. 5 Magnetization curve of FMZ samples fitted with the combined model of the law of approach to saturation and the Langevin function depicting magnetic saturation values.

Table 2 Magnetic characterization values of the FMZ samples

Sample code	M_S (emu g^{-1})	M_{sp} (emu g^{-1})	M_f (emu g^{-1})	H_C (Oe)	M_R (emu g^{-1})
Fe$_3$O$_4$	73.46	73.46	0.19	165.72	8.99
FZ	8.67	8.59	0.09	121.37	1.34
FMZ0.25	18.32	18.25	0.07	86.735	4.65
FMZ0.5	30.80	30.70	0.10	59.74	4.62
FMZ0.75	38.90	38.84	0.06	37.22	2.59
FM	14.72	14.70	0.02	69.35	1.96

applications, such as magnetic hyperthermia. The observed magnetic characteristics values of the FMZ samples are listed in Table 2. Their superparamagnetic behaviour was confirmed by fitting the M–H curves with the combined model incorporating the law of approach to saturation at high field and the Langevin function for the low field saturation curves, described as (eqn (3)),[42] as follows:

$$M_S = M_f \left[1 - \left(\frac{a}{H} \right) - \left(\frac{b}{H^2} \right) \right] + M_{sp} \left[\coth(\alpha H) - \left(\frac{1}{\alpha H} \right) \right] \quad (3)$$

where M_f and M_{sp} are the ferromagnetic and superparamagnetic components of the M_S values, and $\frac{a}{H}$ and $\frac{b}{H^2}$ are the contributions from the structural distortion factor, respectively. The calculated contributions of the ferromagnetic and superparamagnetic components are listed in Table 2. The M_{sp} values are significantly higher than the M_f values, indicating the dominant superparamagnetic nature of the FMZ samples. The ferromagnetic and superparamagnetic components of the Fe$_3$O$_4$ nanoparticles, as the parent system, are also mentioned.

The magnetization of ferrites arises from the antiferromagnetic coupling between their tetrahedral (A) and octahedral (B) sites. In Zn–Mn ferrites, the Zn ions predominantly occupy the tetrahedral sites, while the Mn ions can occupy both the tetrahedral and octahedral sites, depending on the concentration. The net magnetization of the ferrite is the difference between its two interacting sites, A and B, as explained by Néel's collinear spin model of ferrimagnetism.[43] The doping of Zn initially increases the net magnetization due to the weak antiferromagnetic coupling. However, in the case of higher concentrations ($x > 0.5$), the magnetic order collapses, leading to a rapid decrease in magnetization.[44] Thus, with Mn doping, the magnetic nature of Mn^{2+} enhances the net magnetization by contributing more to the B-site. As Mn content increases, the Mn ions occupy the A-site, strengthening the antiferromagnetic coupling, and ultimately reducing the overall magnetization.[16] As observed, for the FMZ0.25, FMZ0.5, and FMZ0.75 samples, the increasing contribution of Mn to the net magnetization through the B site resulted in progressively low, moderate, and high magnetization values, respectively. However, the shift in the Mn ions to the A-sites at a higher Mn content led to stronger antiferromagnetic coupling, ultimately reducing the net magnetization, as observed for the FM sample. In the study by Monisha et al., they reported a similar decrease in saturation
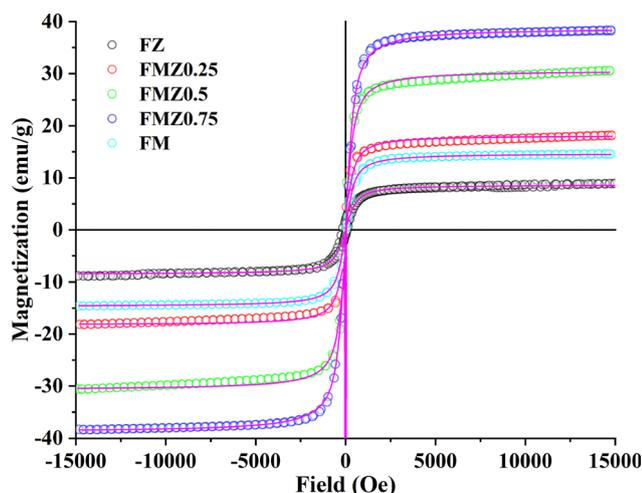
magnetization (0.49 emu g^{-1}) due to the enhanced antiferromagnetic interaction in the Mn-doped Co ferrites.[45] Similarly, the weakened super–exchange interaction in the FZ samples resulted in reduced magnetic moments. Several studies have also reported an initial increase in magnetization with an increase in Zn content, followed by a decrease at higher concentrations.[46–48]

3.6. Heat generation capabilities

The heat generation capabilities of the prepared FMZ samples were assessed using the induction heating method with a field amplitude of 12.89 kA m^{-1} and frequency of 336 kHz. The increase in temperature through the heat generated by the synthesized FMZ samples of various concentrations is illustrated in Fig. 6. The heat generation in superparamagnetic or single-domain MNPs under AMF arises from Néel relaxations and Brownian relaxations due to the response lag. Though these losses are distinct from the classical hysteresis for bulk particles, the relaxation process results in dynamic hysteresis losses, similar to dissipating the energy during the AMF cycle.[49] Relaxation losses are the primary mechanism of heat generation in the MNPs, where magnetic energy is transformed into thermal energy by the applied magnetic field. The Néel and Brownian relaxation mechanisms, involving the rotation of

superspins and the physical rotation of particles, respectively, contribute to heat generation.[50] With a size in the range of 13.61 ± 2.69 to 15.69 ± 3.23 nm, the FMZ samples showed single-domain behaviour, and their heat generation was expected to be governed by the relaxation losses, especially; the Néel relaxation loss.[49] This claim is supported by the superparamagnetic behaviour of the M–H curve, showing negligible H_C and M_R values, and indicating no hysteresis for the FMZ samples. Increasing the solvent temperature in the hyperthermia range (42–47 °C) effectively suggests the suitability of the sample for magnetic hyperthermia.

The heating curve for the FMZ samples was a function of their concentration and magnetization. At 1 mg mL^{-1}, the heating curve of the FMZ0.75 sample was observed to reach up to 42 °C during AMF exposure for 15 min. In comparison, the FMZ0.5 and FMZ0.25 samples raised the temperature to 40.1 °C and 38.6 °C, respectively. The remaining samples, FM and FZ, demonstrated minimal heat generation due to their low magnetization properties. Further, at a concentration of 3 mg mL^{-1}, the FMZ0.75 sample reached hyperthermia temperature within 5 min and exceeded 55.40 °C within 15 min. These obtained values exceed the hyperthermia temperature limits and can be regulated by the regulated application of the alternating field.[51] The FMZ0.5 and FMZ0.25 samples showed
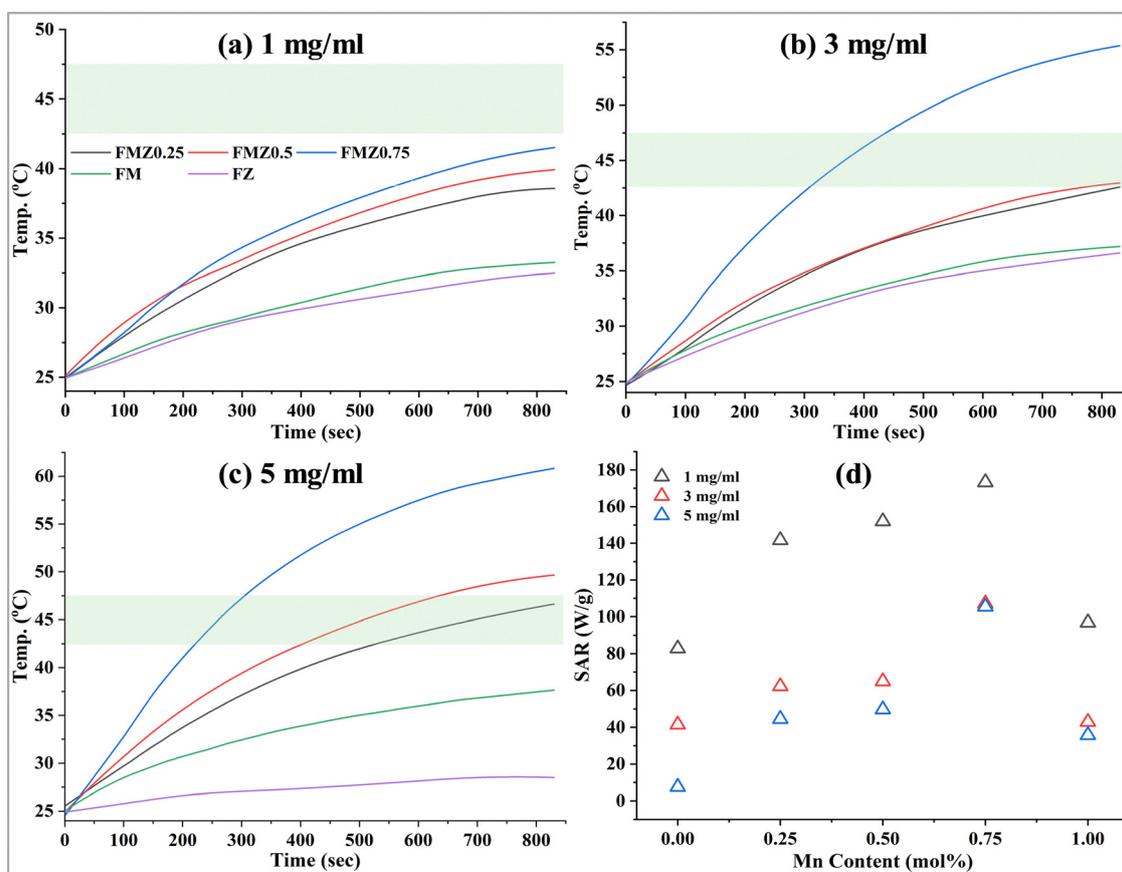

Fig. 6 Increase in the temperature of the medium through the heat generated by FMZ nanoparticles at concentrations of (a) 1 mg mL^{-1}, (b) 3 mg mL^{-1}, and (c) 5 mg mL^{-1} when subjected to an alternating magnetic field, and (d) influence of Mn content on the specific absorption rate values estimated for the FMZ samples.

similar heat curve patterns, reaching the hyperthermia temperature within the duration of AMF exposure. At 5 mg mL^{-1}, the FMZ0.75 sample reached hyperthermia temperature in 3.7 min and peaked at 55.45 °C in 15 min. Similarly, the FMZ0.5 sample took 6.67 min to reach hyperthermia temperature and was elevated to 49.75 °C during exposure. The FMZ0.25 sample attained the desired temperature range in 8.6 min. In contrast, the FM and FZ samples at 3 mg mL^{-1} and 5 mg mL^{-1} failed to reach the therapeutic temperature during the duration of the experiments.

Overall, with an increase in their concentration and magnetization, the heat generation capabilities of the FMZ samples increased. A higher concentration offers more particles for energy absorption and thus greater heat generation. The heating efficiency of the FMZ samples under hyperthermia conditions reflects the strong dependence of SAR on the Mn doping levels, consistent with earlier studies.[52] The higher magnetization value of the FMZ0.75 sample resulted in quicker and more significant heat generation, enabling it to achieve hyperthermia temperatures rapidly. The moderate M_S values of FMZ0.25 and FMZ0.5 resulted in slower heating patterns. At the same time, the inability of the FM and FZ samples to increase the temperature is attributed to their lower magnetic properties.[53]

The heat generation potential of the MNPs is measured in terms of SAR values, which indicate the efficiency of energy absorption from an electromagnetic field. This absorbed energy is subsequently converted to thermal energy, enabling their potential as hypermedia. The heating curves show an initial linear increase in temperature due to the higher energy absorption. The slope of the curve is used to determine the SAR values for the MNPs, given as (eqn (4)):[1]

$$\text{SAR} = C_p\left(\frac{\text{d}T}{\text{d}t}\right)\left(\frac{m_s}{m_m}\right) \quad (4)$$

where C_p is the specific heat capacity of the water (4.186 J g^{-1} K^{-1}), $\left(\frac{\text{d}T}{\text{d}t}\right)$ is the heating rate, and $\left(\frac{m_s}{m_m}\right)$ is the ratio of masses of solvent (here water) and sample. The rate or slope of the heating curve can be determined by the initial section showing a linear increase in temperature or by considering the whole curve. The linear curve method uses an initial short part of the data fitted in the linear equation to determine the slope, while the slope of the entire heating curve is considered for the fitting with the Box–Lucas (BL) equation, given as (eqn (5)):[54]

$$y = a\left(1 - e^{-bx}\right) + c \quad (5)$$

where y is the dependent variable denoting temperature, x is an independent variable such as time, a is the amplitude of the maximum value, b is the rate constant, and c is the offset value for the fitting. The BL equation models the heating dynamics of the curve for MNPs and can be helpful for the optimization of the treatment parameters through the predicted saturation behaviour. The estimated SAR values through the initial linear slope and the BL equation, indicating the heat generation capabilities of the synthesized FMZ samples, are listed in Table 3.

Table 3 Specific absorption rate (SAR) values (W g^{-1}) using the Box–Lucas and linear curve method and intrinsic loss power (ILP) (nH m^2 kg^{-1}) values calculated for the FMZ samples at various sample concentrations

Conc. (mg mL^{-1})	Metrics	FZ	FMZ0.25	FMZ0.5	FMZ0.75	FM
1	SAR_BL	82.81	141.65	151.99	173.24	96.96
	SAR_IC	62.79	108.84	113.02	142.32	62.79
	ILP	1.48	2.54	2.72	3.10	1.74
3	SAR_BL	41.45	62.23	64.92	107.12	42.94
	SAR_IC	29.30	50.23	48.84	87.91	32.09
	ILP	0.74	1.11	1.16	1.92	0.77
5	SAR_BL	7.56	44.55	49.71	105.42	35.70
	SAR_IC	6.70	33.49	41.02	66.98	19.26
	ILP	0.14	0.80	0.89	1.89	0.64

As observed in the heating curves (Fig. 6), the FMZ samples showed decreased SAR values with an increase in their concentration. The observed SAR pattern is likely due to the interparticle interactions at a higher concentration, which influence the magnetic relaxation mechanism. The dipole–dipole coupling, agglomeration, or the chaining of the particles may result in a reduction in the heating efficiency, as indicated by the decreased SAR values. Further, the heat generated through the energy absorption and conversion highlighted the critical role of sample magnetization. The FMZ0.75 sample with the highest M_S value showed comparatively higher SAR values across all concentrations. The SAR values decreased sharply for the moderately magnetized samples, such as FMZ0.25 and FMZ0.5. The FM and FZ samples showed the lowest SAR values amongst the samples, which is attributed to their lower magnetization for all the concentrations. The decrease in the SAR values with an increase in concentration can be related to the magnetic dipole–dipole interactions and the agglomeration effects.[55] The increased density of the MNPs in the system resulted in reduced mobility due to diploe–dipole interactions, and thus relaxation losses for individual particles due to the applied AMF. Also, the local magnetic field arose due to high MNP concentrations, which may have shielded the AMF, reducing the energy absorption of MNPs.[56] Therefore, the optimization process for adequate SAR values desires a suitable concentration at which the magnetic dipole–dipole interactions do not suppress the relaxation movements of the MNPs. In the case of the FMZ0.75 sample, at 1 mg mL^{-1}, its higher SAR value (173.24 W g^{-1}) reflects more efficient heat generation per nanoparticle, but its lower total heat output prevents reaching the hyperthermia temperature range. In contrast, at 3 mg mL^{-1}, despite the reduced SAR value (107.12 W g^{-1}), an increase in concentration results in higher total heat generation, enabling the temperature to exceed the hyperthermia threshold.

Additionally, the differences in the SAR values calculated through the linear slope method and the BL equation were due to the range of the curve considered. The linear slope method considers the initial change in temperature to calculate the slope. However, the assumptions of adiabatic conditions and nonsignificant temperature fluctuations may not occur during

the experiments, causing the underestimation of the SAR values up to 25%.[57] In comparison, the BL equation considers the whole curve when calculating the slope and can be reliable for accurately estimating the SAR values.[54]

Researchers have used different AMF parameter values for heat generation studies, such as field strength and frequency, leading to non-comparable SAR values.[13–15] Therefore, the heating capability of MNPs can be effectively compared across different studies by normalizing the experimental conditions, including the frequency and field strength of the AMF. The normalization termed intrinsic loss power (ILP) (nH m^2 kg^{-1}) can be determined using the following equation (eqn (6)):[55]

$$ILP = \frac{SAR}{H^2 f} \tag{6}$$

ILP allows the comparison of the intrinsic properties of MNPs in terms of heat generation. The calculated ILP values for the FMZ samples are presented in Table 3. Although the ILP values were calculated for comparative assessment, it is important to note that the linear response theory assumes non-interacting superparamagnetic particles. Therefore, the ILP values reported here serve as relative indicators rather than intrinsic material constants.

It was observed that the heating capability of the FMZ samples increased with a higher Mn content, which contributed to enhanced magnetic properties, as discussed. The ILP values of commercial ferrofluids used for magnetic hyperthermia are in the range of 0.05 to 3.0 nH m^2 kg^{-1}.[58] With ILP values in a similar range, the synthesized FMZ samples are suitable for magnetic hyperthermia applications. Therefore, with the highest SAR and ILP values across all the tested concentrations, the FMZ0.75 sample demonstrates superior potential for magnetic hyperthermia applications.

3.7. Correlation of dopant, M_S, and SAR values

The magnetic properties of the MNPs are intricately interrelated, significantly influencing each other. According to the heating curves, it is evident that the SAR values are a function of the magnetization of the sample and exhibit a linear relationship, as shown in Fig. 7a. Additionally, for the single-domain particles, their magnetic properties strongly depend on their particle size, governing both the magnetization and heat generation efficiency. The interplay among the particle size, magnetization, and SAR values for the FMZ samples follows peak-like behavior and can be mathematically described using the following function (eqn (7)):

$$y = y_0 + \frac{4A \cdot e^{-z}}{(1 + e^{-x})^2} \tag{7}$$

$$z = \frac{x - x_c}{w}$$

where x is an input variable, x_c is the maximum for x, w is the width parameter controlling the spread, y_0 is the baseline, A is the amplitude of the peak, e^{-z} is the exponential decay function, and $(1 + e^{-z})^2$ is the term responsible for sigmoidal function behavior. The function highlights the complex size-dependent magnetic and hyperthermia properties of the MNPs, underlining the importance of optimizing their particle size for efficient magnetic hyperthermia performance. According to the well-fitted curves, the parameter x_c corresponds to the optimum particle size for both the maximized M_S and SAR, which was observed to be 14.7 nm (Fig. 7b). Similarly, the Mn content plays a critical role in tuning the magnetic properties, as discussed for the magnetization studies. The relation among the Mn content, M_S, and SAR values of the FMZ samples can be modeled using eqn (7). Based on this relationship, the optimum Mn content for enhanced M_S and SAR values was estimated to be 0.7 mol%, as shown in Fig. S5. Thus, the result emphasizes the strong interdependence between structural and magnetic parameters, emphasizing the significance of tailoring the particle size and Mn content for the optimum magnetic hyperthermia performance of the FMZ nanoparticles.

3.8. Cytocompatibility studies

The suitability of the nanomaterials for biological applications requires proven cytocompatibility assessments. In the initial stages, these assessments are usually carried out through *in vitro* studies; through assays such as cell viability assays.
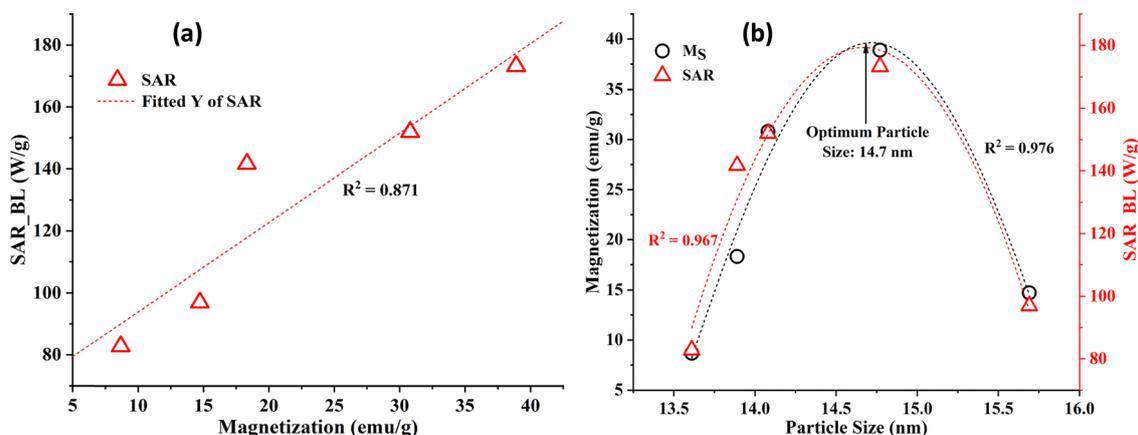

Fig. 7 Correlation between (a) magnetization and SAR values and (b) particle size and magnetization and SAR values.
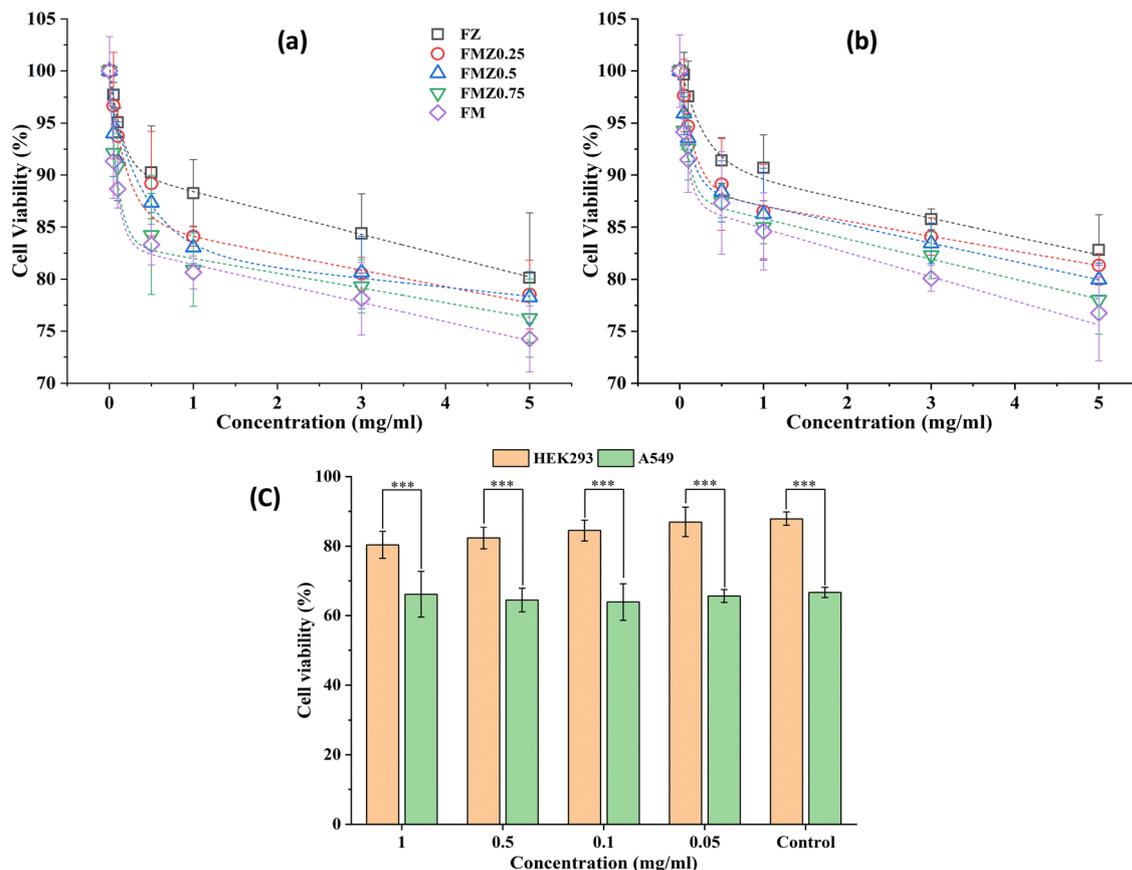
Fig. 8 (a) and (b) *In vitro* cytocompatibility assays for the FMZ samples performed using the HEK-293 cell line for 2 and 4 days, respectively, and (c) cell viability of HEK293 cells and A549 cells incubated with the FMZ0.75 sample at the hyperthermia temperature (45 °C) for 20 minutes (*** p-value > 0.005, 1 : 0.00014, 0.5 : 0.00002, 0.1 : 0.00001, 0.05 : 0.00004 and 0.00002, 0 : 0.00001).

The MTT assay determines the viability of the biological tissues or cells by quantifying the amount of MTT reduced to formazan.[59] The FMZ samples were assessed for their toxic effects on the viability of human embryonic kidney cells (HEK-293) through the MTT assay, as shown in Fig. 8(a) and (b). The FMZ samples demonstrated excellent cytocompatibility at concentrations of 5, 3, 1, 0.5, 0.1, and 0.05 mg mL^{-1} over incubation periods of 2 and 4 days. The cell viability for all FMZ samples remained above the acceptable limits for biomaterials as specified by the ISO 10993-5: 2009 (biological evaluation of medical devices – Part 5: tests for *in vitro* cytotoxicity) regulations.[60]

The results revealed a dose-dependent pattern of cell viability for all the FMZ samples. At the highest concentration of 5 mg mL^{-1}, the average cell viability was approximately 77.50%, while the lowest concentration of 0.05 mg mL^{-1} resulted in a cell viability of nearly 94.37%. The pattern highlighted the beneficial effect of Zn ions across the samples. The FZ sample, with only Zn, showed the highest cell viability for HEK-293 cells, with 80.15% at 5 mg mL^{-1} and 97.73% at 0.05 mg mL^{-1}. The cell viability correspondingly decreased as the Zn content decreased in the FMZ samples. The FMZ0.25, FMZ0.5, and FMZ0.75 samples exhibited cell viabilities of 78.53%, 78.27%, and 76.27%, respectively, at 5 mg mL^{-1}. Similarly, at the lowest

concentration of 0.05 mg mL^{-1}, the cell viabilities were 96.67%, 94.00%, and 92.13% for FMZ0.25, FMZ0.5, and FMZ0.75, respectively. With Mn-only doping, the FM sample exhibited the lowest cell viability, with 74.27% at 5 mg mL^{-1} and 91.33% at 0.05 mg mL^{-1}. After 4 days of incubation, the cell viability increased across all the samples, following a similar trend, and further indicating the positive influence of Zn ions. The FZ sample exhibited a cell viability of 82.82% at 5 mg mL^{-1} and 99.64% at 0.05 mg mL^{-1}, confirming its excellent cytocompatibility. A similar increase in cell viability was observed for the FMZ0.25, FMZ0.5, and FMZ0.75 samples. The FM sample also showed improved cell viability, reaching 79.77% at 5 mg mL^{-1} and 94.13% at 0.05 mg mL^{-1}. The observed cell viability for the FMZ samples over the incubation period and concentration range indicated their potential suitability for biological applications.

Researchers reported that Mn and Zn dopants are cytocompatible and can induce cell growth. Mn-doped iron oxide nanoparticles have been reported to be highly cytocompatible against the HEK-293 and HCT-116 cell lines.[61] Similarly, in the study by de la Fuente-Jiménez *et al.*, they reported the safe cytocompatible nature of Zn ferrite MNPs against HEK-293, MDA-MB-23, and MCF-7 (breast cancer cell lines) with over 75% cell viability.[62] Their study confirmed the non-toxic nature of Zn

ferrites through the crystal violet assay and apoptosis assays, highlighting critical evidence of the cytocompatibility of Zn ferrites for various types of cell lines. Several other studies have reported the cytocompatible nature of Zn ferrites.[63] Mn-doped ferrites have been reported to show excellent cytocompatibility compared to other metal oxide nanoparticles.[64] Similarly, the combined effects of the dopants were studied to be favourable against the BLO-11 (mouse muscle fibroblasts) and BLO-11 and MDA-MB-231 cell lines, confirming the suitability of the FMZ samples for biological applications.[15]

3.9. Hyperthermia studies

Hyperthermia treatment for cancer involves subjecting the infected tissues or cells to elevated temperature in the hyperthermia range of 42–47 °C. This exposure alters the cellular and metabolic processes of cancerous cells and leads to cell death. The primary studies to assess the effects of temperature on the viability of cancer and normal cells were performed on the A549 and HEK-293 cell lines, respectively, at the temperature of 45 °C for 20 minutes simulating hyperthermia conditions. Sample FMZ0.75 at varying concentrations was also incubated with the cells for the experiments to eliminate doubt about its role in the altered cell viability. The resultant cell viability of the HEK-293 and A549 cells after incubating under hyperthermia conditions is shown in Fig. 8c.

As observed, the HEK-293 cells incubated at the hyperthermia temperature (45 °C) exhibited only a slight decrease in cell viability compared to the control cells maintained at 37 °C, highlighting the heat tolerance of the normal cells. Additionally, the cells incubated with varying concentrations of the FMZ0.75 sample showed comparable decreased viability under both normal and hyperthermia conditions. Thus, the role of the FMZ samples in influencing the cell viability under hyperthermia conditions was nullified. Notably, the decreased cell viability remained above the recommended cell viability criteria.[60] In contrast, the A549 cancer cells exposed to hyperthermia at 45 °C displayed significantly decreased cell viability (66%) compared to the cells incubated at 37 °C. Similar observations were found for the cells treated with the FMZ0.75 sample, with the observed viability decreasing to 65% relative to the control cells across all the concentrations under hyperthermia conditions. The consistent reduction in cell viability under hyperthermia conditions highlighted the role of temperature in inducing cell death and eliminated the nanoparticle-related cytotoxicity as a contributing factor. The observed results emphasize the effectiveness of hyperthermia as a specific strategy against cancer cells and are in good agreement with previous studies, which demonstrated the temperature-dependent cytotoxic effects of hyperthermia in cancer therapy.[1,65] A similar decrease in A549 cell viability was reported in the study by Nowicka *et al.*, where Mg-doped iron(III) oxide nanoparticles generated heat under an alternating magnetic field (AMF) for 45 minutes, resulting in less than 25% cell viability remaining.[66]

Hyperthermia temperature leads to protein denaturation and alterations in cytoskeletal structures, resulting in cell cycle arrest. Thus, the generated reactive oxygen species induce necrosis pathways in cancer cells by activating the cell-surface death receptors. As a result, specific cell death signals are transmitted by specific ligands, such as tumor necrosis factor-related apoptosis-inducing ligands (TRAIL). The TRAIL ligand is the inducer of apoptosis in cancer cells, with the least effect on normal cells, resulting in the selective death of cancer cells at hyperthermia temperature compared to normal cells.[67] Normal tissues comprise the developed vascular distribution compared to cancer cells, which prevents tissue damage for a shorter duration.[68] Hence, in this study, no apoptotic effect by the hyperthermia temperature was observed for HEK-293 cells, but the viability of the A549 cells was reduced by up to 60%. Therefore, considering the heat generation capability, the designed material can be used for hyperthermia applications in cancer treatment.

4. Conclusion

Mn–Zn ferrites are widely explored for their versatile electromagnetic properties, making them suitable candidates for applications such as magnetic hyperthermia in cancer therapy. In this study, Mn and Zn-doped ferrites were synthesized using a simple co-precipitation method with varying compositions. The calcined FMZ nanoparticles exhibited a spinel structure, as confirmed by XRD analysis, which showed a redshift in their diffraction patterns. FTIR and Raman spectroscopy revealed interactions between the dopants within the lattice, while XPS analysis confirmed the formation of a mixed spinel structure with tetrahedral and octahedral lattice ion positions. The Mn content significantly influenced the particle size, as supported by the increase in hydrodynamic size and reduced colloidal stability. The magnetization studies demonstrated superparamagnetic behavior with negligible coercivity and remanence. Among the samples, FMZ0.75 exhibited the highest magnetization (38.98 emu g^{-1}), emphasizing the contribution of Mn ions to the magnetic properties. The heat generation studies revealed a concentration-dependent increment, with 3 mg mL^{-1} identified as the optimum concentration, achieving sufficient SAR values to reach the hyperthermia temperature range. The ILP values were comparable to those of commercial MNPs used for hyperthermia. The interrelationship among particle size, magnetization, and SAR values gave a particle size of 14.7 nm and a Mn fraction of 0.7 for the optimized hyperthermia performance. The cytocompatibility tests with HEK-293 cells confirmed the excellent biocompatibility up to a concentration of 5 mg mL^{-1} over four days of incubation. The hyperthermia studies revealed no significant damage to HEK-293 normal cells, while A549 cancer cells showed a decreased viability of 65%, with cancer cell death attributed solely to hyperthermia effects, not the FMZ samples. Owing to their favourable magnetic characteristics, efficient heat generation, and excellent cytocompatibility, the synthesized FMZ samples demonstrate strong potential for magnetic hyperthermia applications.

Author contributions

Conflicts of interest

The authors declare that they have no known competing financial interests or personal relationships that could have appeared to influence the work reported in this paper.

Data availability

The data that support the findings of this study are available upon request.

Supplementary information (SI) is available. See DOI: **https://doi.org/10.1039/d5ma00412h**.

Acknowledgements

References

1 R. Fopase, V. Saxena, P. Seal, J. P. Borah and L. M. Pandey, *Mater. Sci. Eng., C*, 2020, **116**, 111163.

2 J. F. Liu, P. C. Chen, T. Y. Ling and C. H. Hou, *Stem Cell Res. Ther.*, 2022, **13**, 236.

3 Kritika and I. Roy, *Mater. Adv.*, 2022, **3**, 7425–7444.

4 S. Nilawar, M. Uddin and K. Chatterjee, *Mater. Adv.*, 2021, **2**, 7820–7841.

5 L. Wang, A. Hervault, P. Southern, O. Sandre, F. Couillaud and N. T. K. Thanh, *J. Mater. Chem. B*, 2020, **8**, 10527–10539.

6 G. Niraula, C. Wu, X. Yu, S. Malik, D. S. Verma, R. Yang, B. Zhao, S. Ding, W. Zhang and S. K. Sharma, *J. Mater. Chem. B*, 2024, **12**, 286–331.

7 D. García-Soriano, P. Milán-Rois, N. Lafuente-Gómez, C. Rodríguez-Díaz, C. Navío, Á. Somoza and G. Salas, *J. Colloid Interface Sci.*, 2024, **670**, 73–85.

8 S. Choudhury, A. Joshi, D. Dasgupta, A. Ghosh, S. Asthana and K. Chatterjee, *Mater. Adv.*, 2024, **5**, 3345–3356.

9 K. Raju, G. Venkataiah and D. H. Yoon, *Ceram. Int.*, 2014, **40**, 9337–9344.

10 S. Jovanović, N. Yaacoub, S. Slimani, M. M. Kržmanc, M. Vukomanović, M. Spreitzer, D. Peddis and A. Omelyanchik, *J. Chem. Phys.*, 2024, **161**.

11 G. Thirupathi and R. Singh, *IEEE Trans. Magn.*, 2014, **50**, 1–4.

12 R. Santhiya and A. R. Kumar, *J. Therm. Biol.*, 2024, 103936.

13 L. B. De Mello, L. C. Varanda, F. A. Sigoli and I. O. Mazali, *J. Alloys Compd.*, 2019, **779**, 698–705.

14 G. Nandhini and M. K. Shobana, *Mater. Today Commun.*, 2024, **39**, 109046.

15 A. Manohar, V. Vijayakanth, K. Chintagumpala, P. Manivasagan, E. S. Jang and K. H. Kim, *Colloids Surf., A*, 2023, **675**, 132037.

16 B. Kakavandi, A. Jonidi, R. Rezaei, S. Nasseri, A. Ameri and A. Esrafily, *Iran. J. Environ. Health Sci. Eng.*, 2013, **10**, 1–9.

17 P. Shahi, H. Singh, A. Kumar, K. K. Shukla, A. K. Ghosh, A. K. Yadav, A. K. Nigam and S. Chatterjee, *AIP Adv.*, 2014, **4**, 097137.

18 R. E. El-Shater, H. El Shimy, S. A. Saafan, M. A. Darwish, D. Zhou, K. C. B. Naidu, M. U. Khandaker, Z. Mahmoud, A. V. Trukhanov, S. V. Trukhanov and F. Fakhry, *Mater. Adv.*, 2023, **4**, 2794–2810.

19 D. Nagao, J. Fukushima, Y. Hayashi and H. Takizawa, *Ceram. Int.*, 2015, **41**, 14021–14028.

20 R. Rajalakshmi and N. Ponpandian, *Mater. Res. Bull.*, 2023, **164**, 112242.

21 P. Soltanpour, R. Naderali and K. Mabhouti, *Sci. Rep.*, 2024, **14**, 21287.

22 S. Thota, S. C. Kashyap, S. K. Sharma and V. R. Reddy, *J. Phys. Chem. Solids*, 2016, **91**, 136–144.

23 C. Murugesan and G. Chandrasekaran, *J. Supercond. Novel Magn.*, 2016, **29**, 2887–2897.

24 H. Etemadi and P. G. Plieger, *J. Mater. Sci.*, 2021, **56**, 17568–17583.

25 G. Channagoudra, A. K. Saw and V. Dayal, *J. Phys. Chem. Solids*, 2021, **154**, 110086.

26 Z. Y. Xu, J. L. Fan, S. Q. Zhao, H. B. Zhang, F. C. Yin, Y. Han and T. Liu, *J. Alloys Compd.*, 2020, **835**, 155285.

27 C. A. P. Gómez, C. A. B. Meneses and J. A. Jaén, *J. Magn. Magn. Mater.*, 2020, **505**, 166710.

28 D. Varshney, K. Verma and A. Kumar, *Mater. Chem. Phys.*, 2011, **131**, 413–419.

29 M. Testa-Anta, M. A. Ramos-Docampo, M. Comesana-Hermo, B. Rivas-Murias and V. Salgueirino, *Nanoscale Adv.*, 2019, **1**, 2086–2103.

30 R. Gupta, R. Tomar, S. Chakraverty and D. Sharma, *RSC Adv.*, 2021, **11**, 16942–16954.

31 Z. H. Ye, Z. X. Deng, L. Zhang, J. N. Chen, G. W. Wang and Z. P. Wu, *Mater. Res. Express*, 2020, **7**, 035007.

32 M. L. Li, H. Y. Fang, H. L. Li, Y. Y. Zhao, T. R. Li, H. B. Pang, J. Tang and X. S. Liu, *J. Supercond. Novel Magn.*, 2017, **30**, 2275–2281.

33 H. Qin, Y. Yang, W. Shi and Y. She, *Environ. Sci. Pollut. Res. Int.*, 2021, **28**, 26558–26570.

34 W. Azouzi, I. Boulahya, J. Robert, A. Essyed, A. Mahmoud, A. Al Shami, D. Ihiawakrim, H. Labrim and M. Benaissa, *Ultrason. Sonochem.*, 2024, **111**, 107108.

35 Y. Guo, N. Zhang, X. Wang, Q. Qian, S. Zhang, Z. Li and Z. Zou, *J. Mater. Chem. A*, 2017, **5**, 7571–7577.

36 A. A. de Almeida, F. Fabris, G. S. da Silva, K. R. Pirota, M. Knobel and D. Muraca, *ACS Appl. Mater. Interfaces*, 2025, **17**, 13083–13093.

37 P. C. Patil, A. A. Gaikwad, V. P. Phase, R. H. Kadam, S. E. Shirsath and J. J. Chamargore, *Ceram. Int.*, 2025, **51**(16), 21675–21688.

38 K. Kogulakrishnan, S. Nithiyanantham, R. Mohan, N. V. Giridharan, S. Silambarasan, A. Venkadesh, V. Latha, B. Gunasekaran and L. Palaniappan, *J. Mol. Struct.*, 2025, **1321**, 140026.

39 M. Li, W. Wang and C. Xu, *Chem. Eng. Process.*, 2025, **208**, 110134.

40 S. Nasrin, F. U. Z. Chowdhury and S. M. Hoque, *Phys. B*, 2019, **561**, 54–63.

41 J. N. Israelachvili, *Intermolecular and Surface Forces*, Academic press, 3rd edn, 2011.

42 K. P. Hazarika, R. Fopase, L. M. Pandey and J. P. Borah, *Phys. B*, 2022, **645**, 414237.

43 J. M. D. Coey, *Phys. Rev. Lett.*, 1971, **27**, 1140.

44 P. V. V. Romanholo, T. E. P. Alves, J. Swapnalin, P. Banerjee and A. J. R. Franco, *Mater. Chem. Phys.*, 2022, **284**, 126072.

45 P. Monisha, P. Priyadharshini, S. S. Gomathi and K. Pushpanathan, *J. Phys. Chem. Solids*, 2021, **148**, 109654.

46 B. Dey, C. Manoharan, M. Venkateshwarlu, C. S. Pawar and S. Sagadevan, *Ceram. Int.*, 2024, **50**, 12121–12135.

47 Y. Hadadian, D. R. T. Sampaio, A. P. Ramos, A. A. O. Carneiro, M. Mozaffari, L. C. Cabrelli and T. Z. Pavan, *J. Magn. Magn. Mater.*, 2018, **465**, 33–43.

48 X. Li, E. Liu, Z. Zhang, Z. Xu and F. Xu, *J. Mater. Sci.: Mater. Electron.*, 2019, **30**, 3177–3185.

49 S. V. Jadhav, P. S. Shewale, B. C. Shin, M. P. Patil, G. D. Kim, A. A. Rokade, S. S. Park, R. A. Bohara and Y. S. Yu, *J. Colloid Interface Sci.*, 2019, **541**, 192–203.

50 Z. Shaterabadi, G. Nabiyouni and M. Soleymani, *Prog. Biophys. Mol. Biol.*, 2018, **133**, 9–19.

51 C. Martins, C. Rolo, V. R. G. Cacho, L. C. J. Pereira, J. P. Borges, J. C. Silva, T. Vieira and P. I. P. Soares, *Mater. Adv.*, 2025, **6**, 1726–1743.

52 D. García-Soriano, R. Amaro, N. Lafuente-Gómez, P. Milán-Rois, Á. Somoza, C. Navío, F. Herranz, L. Gutiérrez and G. Salas, *J. Colloid Interface Sci.*, 2020, **578**, 510–521.

53 I. D. Shabalkin, A. S. Komlev, S. A. Tsymbal, O. I. Burmistrov, V. I. Zverev and P. V. Krivoshapkin, *J. Mater. Chem. B*, 2023, **11**, 1068–1078.

54 R. R. Wildeboer, P. Southern and Q. A. Pankhurst, *J. Phys. D: Appl. Phys.*, 2014, **47**, 495003.

55 Nitu, R. Fopase, L. M. Pandey, K. P. Hazarika, J. P. Borah, R. K. Singh and A. Srinivasan, *J. Mater. Chem. B*, 2024, **12**, 3494–3508.

56 I. Morales, A. Koch, C. Wesemann, R. T. Graf and N. C. Bigall, *Nanoscale*, 2025, **17**, 5993–6003.

57 I. M. Obaidat, V. Narayanaswamy, S. Alaabed, S. Sambasivam and C. V. V. M. Gopi, *Magnetochemistry*, 2019, **5**, 67.

58 O. L. Lanier, O. I. Korotych, A. G. Monsalve, D. Wable, S. Savliwala, N. W. F. Grooms, C. Nacea, O. R. Tuitt and J. Dobson, *Int. J. Hyperthermia*, 2019, **36**, 687–701.

59 J. C. Stockert, R. W. Horobin, L. L. Colombo and A. Blázquez-Castro, *Acta Histochem.*, 2018, **120**, 159–167.

60 W. Li, J. Zhou and Y. Xu, *Biomed. Rep.*, 2015, **3**, 617–620.

61 T. M. Alfareed, Y. Slimani, M. A. Almessiere, M. Nawaz, F. A. Khan, A. Baykal and E. A. Al-Suhaimi, *Sci. Rep.*, 2022, **12**, 14127.

62 J. L. de la Fuente-Jiménez, C. I. Rodríguez-Rivas, I. B. Mitre-Aguilar, A. Torres-Copado, E. A. García-López, J. Herrera-Celis, M. G. Arvizu-Espinosa, M. A. Garza-Navarro, L. G. Arriaga and J. L. García, *Int. J. Mol. Sci.*, 2023, **24**, 12860.

63 L. G. Beslin and A. R. Arya, *J. Biomed. Res. Environ. Sci.*, 2024, **2766**, 2276.

64 N. Hashemi, S. Naderlou, A. Mohammadi and H. Danafar, *Mater. Adv.*, 2025, **6**, 2925–2941.

65 S. Deka, V. Saxena, A. Hasan, P. Chandra and L. M. Pandey, *Mater. Sci. Eng., C*, 2018, **92**, 932–941.

66 A. M. Nowicka, M. Ruzycka-Ayoush, A. Kasprzak, A. Kowalczyk, M. Bamburowicz-Klimkowska, M. Sikorska, K. Sobczak, M. Donten, A. Ruszczynska and J. Nowakowska, *J. Mater. Chem. B*, 2023, **11**, 4028–4041.

67 K. Ahmed, Y. Tabuchi and T. Kondo, *Apoptosis*, 2015, **20**, 1411–1419.

68 S. Masunaga, H. Nagasawa, Y. Uto, H. Hori, M. Suzuki, K. Nagata, Y. Kinashi and K. Ono, *Int. J. Hyperthermia*, 2005, **21**, 305–318.